TOWARDS AN ANALYSIS OF THE LIQUID-WATER FRACTION FOR OROGRAPHIC PRECIPITATION

W. Massey Bartolini[1,2] and Heather D. Reeves[3]

[1]National Weather Center Research Experiences for Undergraduates Program
Norman, Oklahoma
[2]University of North Carolina at Asheville
Asheville, North Carolina
[3]University of Oklahoma Cooperative Institute for Mesoscale Meteorological Studies
& NOAA National Severe Storms Laboratory
Norman, Oklahoma

ABSTRACT

Knowing the liquid-water fraction (LWF) in the rain/snow transition zone has useful applications in hydrology, road transportation, and aviation. Several control parameters that dictate the LWF are identified through a series of idealized, two-dimensional experiments using a spectral-bin microphysical model. These are the stability, the drop-size distribution (DSD), and the degree of riming (RF). The most important of these is stability. Though DSD and RF have secondary impacts, they are still non-negligible. In real case studies, stability can be determined from numerical-model output, but DSD and RF are unknown. Therefore, several sets of experiments are conducted to gauge the effects of DSD and RF variations on the rain/snow transition zone for actual case studies of orographic precipitation in the western United States. Each experiment uses a unique combination of DSD and RF, which are assumed to be constant across the entire domain. These experiments show that DSD and RF have nontrivial effects on the LWF and depth of the rain/snow transition zone. In some case studies, the depth of the transition zone varies by as much as 450 m.

1. INTRODUCTION

The rain/snow (RASN) transition zone is a primary focus for studies of winter precipitation, especially when considering the precipitation-type transition in complex terrain or along-mountain environments. One geographic area of interest is central California, where landfalling coastal storms transport copious amounts of moisture towards the steep terrain of the northern Sierra Nevada Mountains during the winter season. Knowledge of the location and characteristics of the RASN transition zone is very important, as the physical differences between snow accumulations and rainfall runoff affect streamflow and storm flooding, among other applications (White et al. 2002, Lundquist et al. 2008).

[1] *Corresponding author address:*
Massey Bartolini
University of North Carolina at Asheville,
Department of Atmospheric Sciences,
CPO #2450, UNC Asheville, One University Heights,
Asheville, NC, 28804-8511
masseybartolini@gmail.com

Previous studies have analyzed the RASN transition zone using a variety of observations and methods. For example, Lundquist et al. (2008) used radar profilers to measure the brightband heights to compare with surface temperature observations. Their results provide insight on melting layer variations due to diabatic processes. Other work by Martner et al. (2008) compared disdrometer observations and periods of bright banding versus non-bright banding in radar observations, to provide a climatology of these two precipitation regimes and the associated impacts on quantitative precipitation estimates in northern California. Minder and Kingsmill (2013) analyze the upwind and near-terrain melting layer using radar brightband observations and show similar results. Their work also considers microphysics schemes in high-resolution numerical modeling, as well as air parcel trajectories, to provide detailed information about other mountainside RASN transition controls for a single case study. Other modeling of orographic flow influences (Minder et al. 2011) shows some of the variability associated with the RASN transition zone in different flow regimes (e.g., terrain-blocked flow).

While some of the general controls of the melting layer have been studied, the details and characteristics of the RASN transition zone itself and the liquid-water fraction (LWF) at the surface are

somewhat unknown. This study uses a simplified spectral-bin microphysical model to quantify the effects of several environmental factors such as drop-size distribution (DSD) and riming factor (RF) on the RASN transition zone. The model used in this paper will be introduced in Section 2, and results for several key parameters analyzed will be described in Section 3. A discussion of the RASN transition-zone variability using several winter storm case studies will follow in Section 4, with this study's conclusions detailed in Section 5.

2. SPECTRAL BIN CLASSIFIER

A simple microphysical model [the spectral-bin classifier (SBC); Reeves et al. 2015] is used to create an analysis of the RASN transition zone. The SBC calculates the LWF of hydrometeors falling from the cloud top to the surface, for a spectrum of drop sizes. It accounts for both melting and refreezing and requires the user to provide an initial RF, ice nucleation temperature (T_{ice}), DSD, and thermodynamic profile. The SBC does not allow for hydrometeor interactions (i.e., aggregation) or growth or decay (i.e., sublimation or deposition). In other words, one hydrometeor aloft produces one hydrometeor at the surface.

An example of the SBC output is provided in Fig. 1. The thermodynamic input used for this example is the observed sounding from Oakland, California at 0000 UTC 3 March 2014 (Fig. 1a). This sounding crosses the 0° isotherm at about 1700 m above ground level (AGL). Assuming the cloud top has minimum temperatures that are less than T_{ice}, all hydrometeors will start out as initially frozen. When they reach the 0° isotherm, they will begin to melt. Complete melting of the hydrometeors will occur some distance below the 0° isotherm. While very small hydrometeors melt almost instantaneously, larger ones take longer to melt. Fig. 1b shows the LWF according to the SBC, assuming RF=1 and drop sizes that range from 0.01 mm to 5.85 mm. The region between LWF=0 and LWF=1 is the RASN transition zone, and its vertical thickness is the depth of the melting layer (D_{melt}). As indicated, D_{melt} is approximately 250 meters for a 1.8 mm drop size, but increases to about 900 meters for hydrometeors with a drop size of about 5.6 mm.

3. CONTROL PARAMETERS FOR D_{melt}

In this simplified construct, there are only three variables that affect D_{melt}. These are stability (S), DSD, and RF, with each affecting the LWF of a falling hydrometeor in different ways. For example, an input sounding with a given stability (red line in Fig. 2a) will cause D_{melt} to be a certain depth. If the stability is changed (blue line in Fig. 2a), then the depth of the melting layer will also change. In this case, the increased stability leads to a decreased mean-layer temperature for the profile region warmer than the 0° isotherm. This, in turn, will cause melting to occur

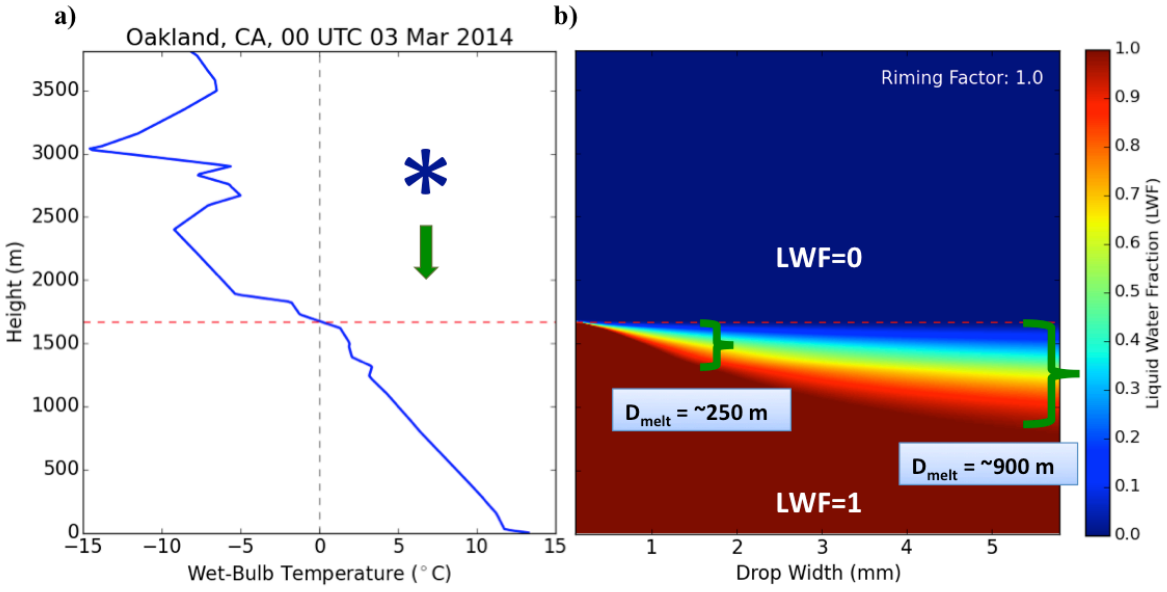

FIG. 1: (a) 0000 UTC 3 March 2014 observed sounding from Oakland, CA, and (b) corresponding spectral-bin classifier plot of the liquid-water fraction

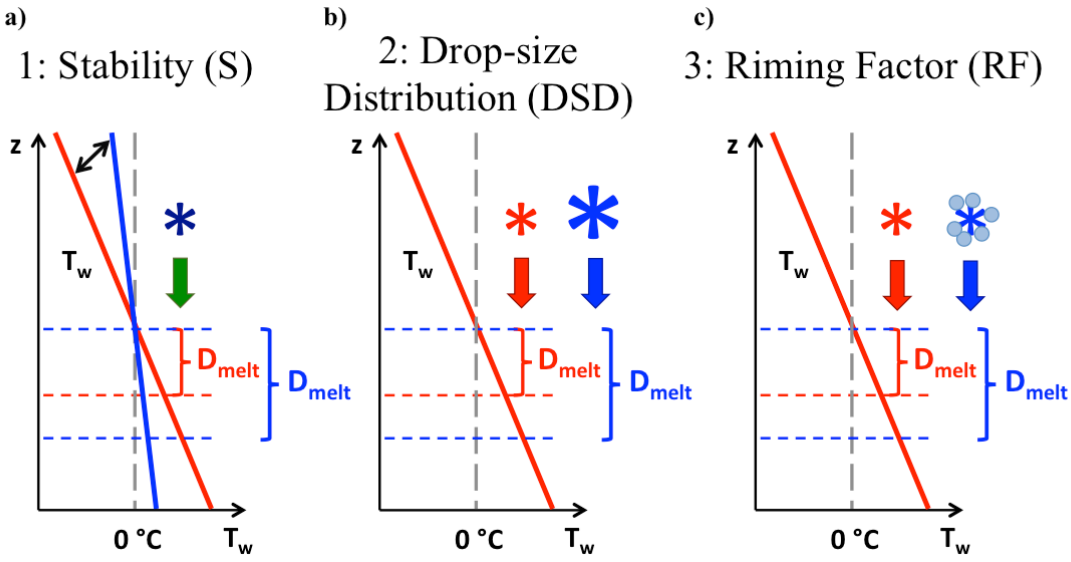

FIG. 2: Diagrams showing changes in melting layer depth due to variations in (a) stability, (b) drop-size distribution, and (c) riming factor

more slowly, and will therefore increase D_{melt}. Next, the effects of the drop size on D_{melt} are illustrated in Fig. 2b. All else being equal, smaller hydrometeors require less time for melting and, therefore, have a smaller D_{melt}.

Finally, the RF will also affect the depth of the melting layer. Let us assume the two hydrometeors in Fig. 2c have the same mass — their only difference is the degree of riming. By virtue of its lower density and higher ventilation coefficient, the pristine, unrimed crystal (red snowflake, Fig. 2c) will take less time to melt, thus resulting in a shallower D_{melt}, as illustrated in Fig. 2c. According to the above logic, D_{melt} is proportional to DSD and RF, and is inversely proportional to S. The reader may note that S, DSD, and RF are not completely independent of one another. As S decreases, the vertical velocity will increase, leading to higher DSDs and RFs. However, knowledge of S alone does not provide precise guidance on the values of DSD and RF, as other factors also control these variables. Since all three variables are independently specified in the SBC, they are treated as independent for the purposes of this study.

3.1 *Methods/Experiment Design*

How much do each of the parameters discussed above affect D_{melt}? To answer this, a number of idealized experiments are performed, wherein each of the three primary parameters are independently varied. For these experiments, nine idealized, thermodynamic profiles are used (Fig. 3a). For simplicity, each profile is assumed to be saturated, has a constant lapse rate, and crosses the 0 °C isotherm at the same altitude. For the nine profiles, the stability ranges from 1 °C km^{-1} to 9 °C km^{-1}. Each profile is referred to by its lapse rate.

Similarly, nine idealized DSDs are tested, based off of the gamma distribution (Fig. 3b). For this study, the gamma distribution used is representative of Joss RD-80 impact disdrometer observations from Cazadero, California (see Fig. 8a for location). The gamma distribution scale parameter is fixed at 0.25 while the shape parameter is varied from 1–9 to create nine different DSDs. Each DSD is labeled by its shape parameter in Fig. 3b. These idealized gamma distributions are scaled vertically by a factor of 5000 to match the summed hourly hydrometeor counts from the Cazadero disdrometer. The binned drop counts are representative of moderate precipitation rates (~30–35 dBZ) at Cazadero. Finally, nine riming factor values, ranging from 1 (a pristine, unrimed hydrometeor) to 5 (a completely obscured graupel particle), are considered (Fig. 3c).

To provide consistent measurements of D_{melt} for all experiments, D_{melt} is calculated at the 75th percentile of the DSD for each experiment because D_{melt} varies with hydrometeor size (see Fig. 1b). For example, the 75th percentile of DSD=9 is shown in Fig. 3b. This percentile is chosen as a threshold because it shows most of the D_{melt} variability associated with a given DSD.

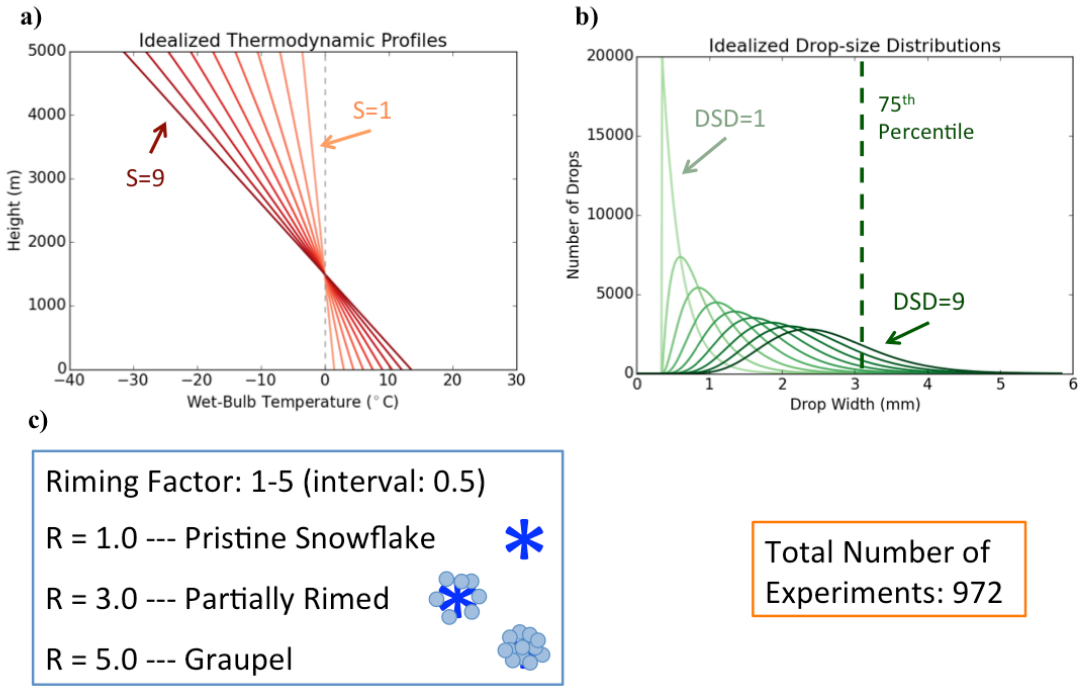

FIG. 3: Idealized range of parameters used in the spectral-bin classifier: (a) nine thermodynamic profiles, (b) nine drop-size distributions, and (c) nine riming factor values.

3.2 *Stability*

Let us first consider D_{melt} as a function of only S and RF. In these experiments, DSD=3.5. For all experiments, D_{melt} decreases as stability decreases (Fig. 4a). The greatest sensitivity occurs for environments with comparatively low S. Note that as S increases from 1 °C km^{-1} to 2 °C km^{-1}, D_{melt} decreases by about 400 m, but as S increases from 8 °C km^{-1} to 9 °C km^{-1}, D_{melt} only changes by about 50 m. This is true regardless of the RF used.

The same analysis is repeated, only this time RF is held constant (RF=2.5) and DSD is varied (Fig. 4b). In these experiments, there is more spread between the curves than in Fig. 4a. This indicates that DSD exerts a stronger control on D_{melt} than does RF, but the same overall patterns emerge. Namely, as S increases, D_{melt} decreases and the change in D_{melt} with changing S is more pronounced for lower-stability environments.

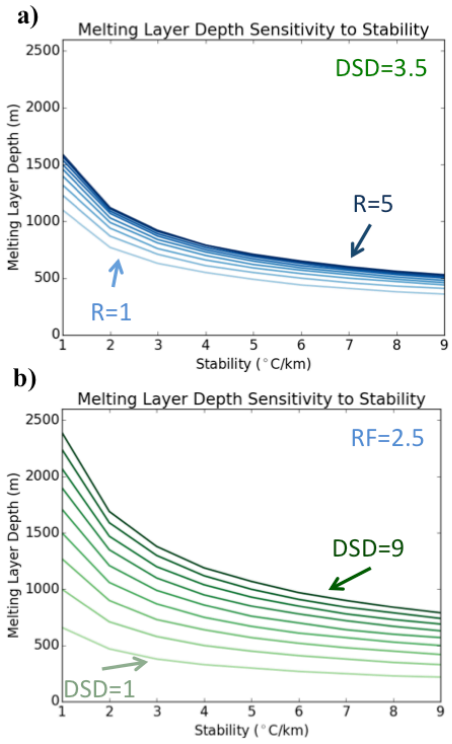

FIG. 4: Sensitivity plots of melting layer depth as a function of stability, for nine different values of (a) riming factor and (b) drop-size distribution

3.3 *Drop-size Distribution*

A similar series of experiments is conducted to explore D_{melt} variability due to DSD changes, as S and then RF are each held constant (S=5.5 °C km^{-1} and RF=2.5). In every experiment, D_{melt} increases as the DSD increases (Figs. 5a and 5b). This sensitivity is slightly stronger for DSDs ranging from 1 to 3. As one would expect, the spread between the curves in Fig. 5b is greater than in Fig. 5a — an indication of the stronger control S has on D_{melt} relative to RF.

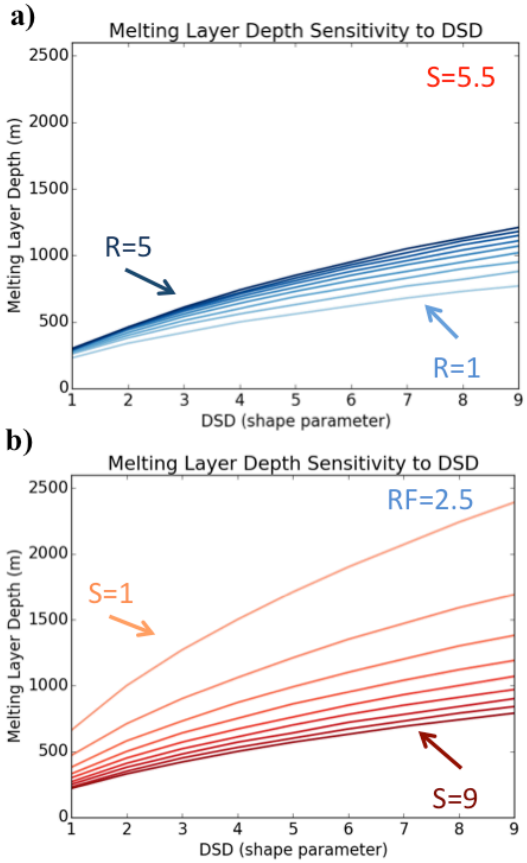

FIG. 5: Sensitivity plots of melting layer depth as a function of drop-size distribution, for nine different values of (a) riming factor and (b) stability

3.4 *Riming Factor*

Likewise, D_{melt} variability due to RF is shown in Fig. 6. These experiments assume either a constant DSD (DSD=3.5, Fig. 6a) or S (S=5.5 °C km^{-1}, Fig. 6b). As RF increases, D_{melt} also increases, with the most sensitivity occurring for RF ≤ 2. The overall spread of the line plots is similar for both DSD and S, but the spread in Fig. 6b is more intriguing. Unlike some figures (Figs. 5a, 6a) where all curves are nearly equally spaced, as S increases, the separation between adjacent curves in Fig. 6b decreases. As in Fig. 4, this suggests D_{melt} is more sensitive to control parameter changes in environments with low S. Also, the difference in D_{melt} between the experiments with S=1 °C km^{-1} and S=9 °C km^{-1} is much greater than the difference in D_{melt} between RF=1 and RF=5 for any one curve. This is again indicative of the strong control S has on D_{melt} relative to both DSD and RF.

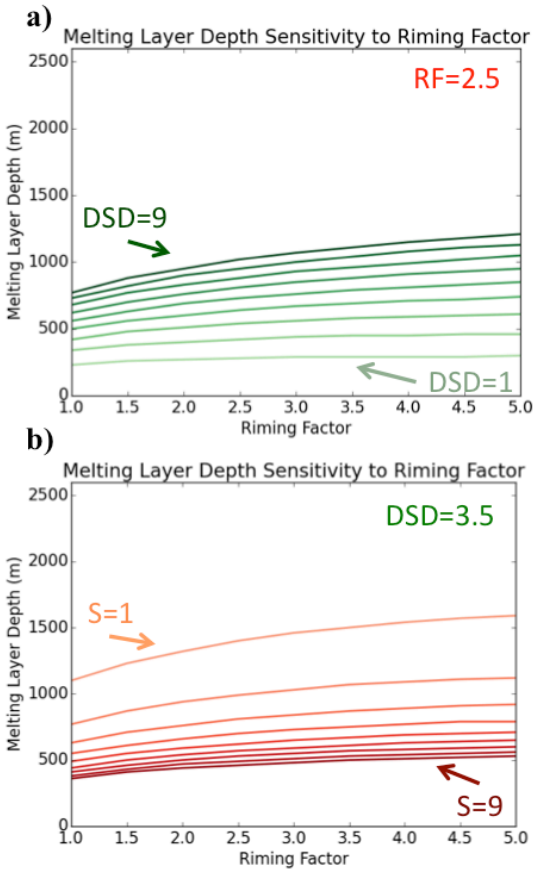

FIG. 6: Sensitivity plots of melting layer depth as a function of riming factor, for nine different values of (a) drop-size distribution and (b) stability

3.5 *Sensitivity Comparison and Summary*

The above results are summarized in the phase-space diagrams in Fig. 7. In each diagram, two parameters are varied while the third is held constant, with D_{melt} plotted for each unique combination. The constant value for the third D_{melt} controls are RF=2.5, DSD=3.5, and S=5.5 °C km^{-1} for Figures 7a, 7b, and 7c, respectively. Salient differences in the control

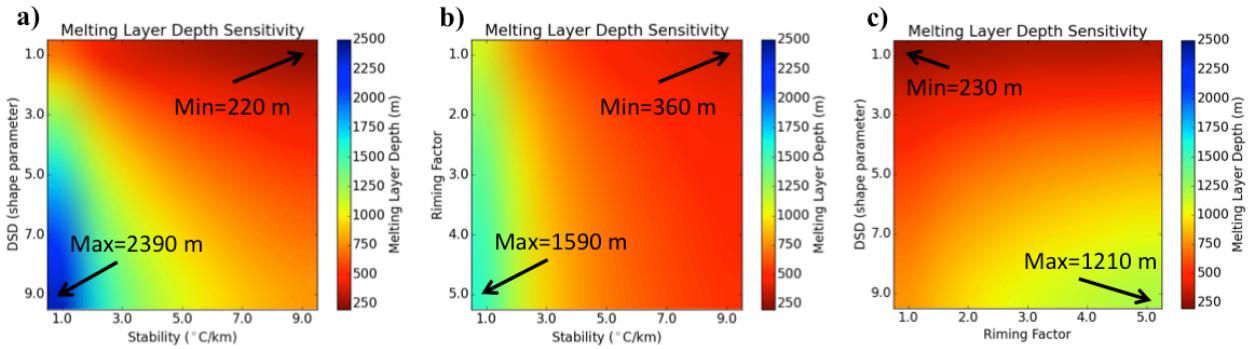

FIG. 7: Phase-space diagrams of melting layer depth for: (a) stability and drop-size distribution, (b) stability and riming factor, and (c) riming factor and drop-size distribution

parameters' influence on D_{melt} are quite obvious in this analysis.

Overall, a representative D_{melt} range can be quantified for each control parameter by computing the D_{melt} variation at the median value of the second control in each phase-space diagram. These experiments show that S, DSD, and RF can change D_{melt} by approximately 1060 m, 775 m, and 255 m, respectively. Hence, S is the most important control on D_{melt}, but changes in D_{melt} due to RF and DSD are still non-negligible.

Figs. 7a and 7b also show an example of an interaction between variations of two parameters. For the specific case of a high-S environment (S=1 °C km^{-1}), RF and DSD cause larger variations in D_{melt}. D_{melt} variability due to DSD variations for S=1 °C km^{-1} increased to 1730 m from the overall average of 775 m. Similarly, D_{melt} variability due to RF changes for S=1 °C km^{-1} increased to 480 m from the overall average of 255 m. This is just one example where specific combinations of two parameters have an additive effect on D_{melt} variations.

4. CASE STUDY DISCUSSION

With the impacts of the three primary D_{melt} parameters quantified, one can now turn to actual case studies to see how these parameters affect the LWF in complex terrain. For example, do DSD and RF variations still affect the LWF, even though they are less important parameters as shown in the idealized experiments above? This question and other impacts will be discussed using several recent case studies from the 2013–2014 winter season.

Figure 8 shows 0200 UTC 7 December 2013, from the early part of a very cold synoptic system

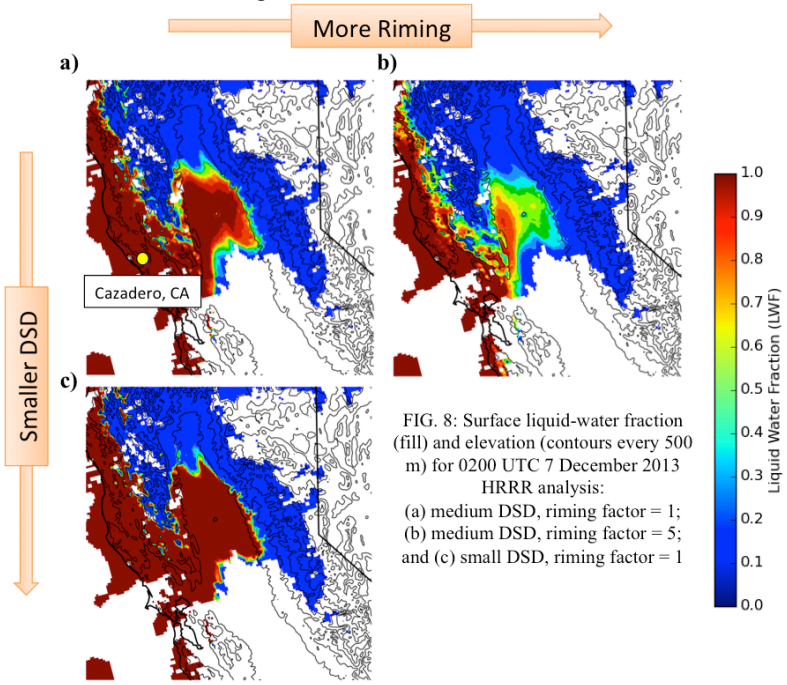

FIG. 8: Surface liquid-water fraction (fill) and elevation (contours every 500 m) for 0200 UTC 7 December 2013 HRRR analysis: (a) medium DSD, riming factor = 1; (b) medium DSD, riming factor = 5; and (c) small DSD, riming factor = 1

moving through northern California. For these analyses, the SBC is modified to read in High-Resolution Rapid Refresh (HRRR) model thermodynamic profiles for every gridpoint within the domain, at a resolution of 3 km. As before, the SBC calculates the LWF from the cloud top down to the surface for each gridpoint, using the corresponding thermodynamic profile information from the 0-hr HRRR analysis. For each of the three plots shown, a uniform DSD and riming factor (RF) value for the entire domain are input into the SBC. Shown in Figs. 8,9 is the summed LWF across the entire DSD at the surface.

Instead of idealized DSDs based on the gamma distribution, two actual DSDs from the Cazadero disdrometer are used: a medium DSD from 0000 UTC 4 March 2014 (similar to an idealized DSD of 3.5) and a small DSD from 0600 UTC 28 March 2014 (similar to an idealized DSD of 1). Figure 8a represents the DSD weighted towards medium-sized hydrometeors and RF=1 with Figure 8b using the same DSD and RF=5. Figure 8c represents a DSD weighted towards very small hydrometeors and RF=1. In other words, RF increases from left to right (Fig. 8a to Fig. 8b), and DSD decreases from top to bottom (Fig. 8a to Fig. 8c).

In Figures 8a–8c, a significant amount of LWF variability is evident. While the entire spectrum of possibilities ranging from a sharp rain/snow transition in Figure 8c to a diffuse transition in Figure 8b is unlikely, these plots show that changes in DSD and RF are still important over a region of complex terrain.

The next case study is from 1400 UTC 28 February 2014, associated with a relatively warmer and stronger synoptic system. For this case, the same three variations of DSD and RF are used. Figures 9a–9c highlight the Feather River Basin in the northern Sierra Nevada. At a river-basin scale, significant precipitation-type variability is possible over a spectrum of these solutions.

Between the two extremes (Figs. 9b and 9c), the bottom of the melting layer descends approximately 450 m in elevation, covering the Feather River Basin in more of a frozen precipitation outcome in Figure 9b than in Figure 9c. As in the previous case study, even with LWF variation constrained to changes in DSD and RF alone, the large range of possible outcomes indicates that both control parameters are important in actual precipitation events.

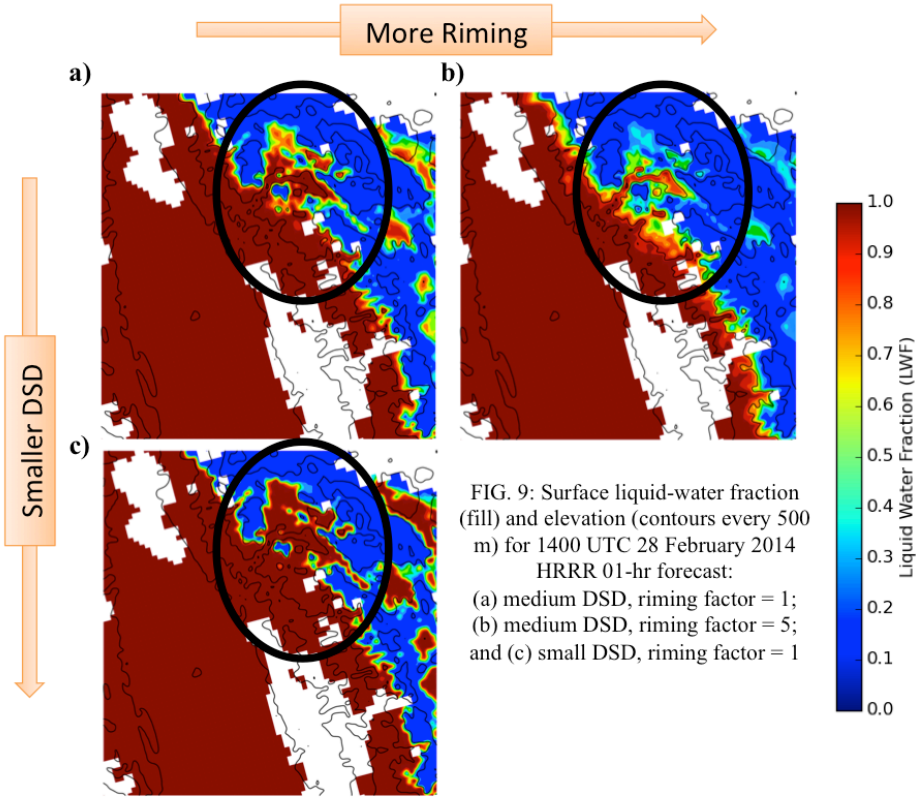

FIG. 9: Surface liquid-water fraction (fill) and elevation (contours every 500 m) for 1400 UTC 28 February 2014 HRRR 01-hr forecast: (a) medium DSD, riming factor = 1; (b) medium DSD, riming factor = 5; and (c) small DSD, riming factor = 1

5. CONCLUSIONS

Using the spectral bin classifier (SBC), the three parameters that affect the depth of the melting layer (D_{melt}) are quantified. These parameters are stability, drop-size distribution, and riming factor (S, DSD, and RF). The idealized SBC tests show that S has the most influence on D_{melt}, with DSD and RF as secondary controls. Specifically, D_{melt} changes by approximately 1060 m, 775 m, and 255 m, when considering S, DSD, and RF individually. However, the case studies discussed demonstrate that DSD and RF variations alone have significant influence over the spatial characteristics of the along-mountain rain/snow (RASN) transition zone. The sensitivity of D_{melt} to all three parameters is important for many aspects of hydrology, mountain meteorology, and related fields.

For example, the variability between the DSD and RF experiments for the 28 February 2014 case indicates a variety of possible outcomes (from mostly accumulating frozen precipitation to mostly liquid precipitation and runoff) for an application like stream-flow forecasting. White et al. (2002) found that changing the RASN transition zone by about 610 m for several river basins in northern California would triple the amount of runoff into the rivers. Therefore, finding a 450 m difference in D_{melt} between the two most extreme experiments for the 28 February 2014 case study is very significant for hydrologic applications.

From an idealized perspective, this study provides information about some parameters affecting D_{melt}. However, to better understand D_{melt} and LWF variability over spatial and temporal scales in real case studies, more precise information about the SBC input parameters must be obtained. Even if high-resolution models (e.g., HRRR) depict near-terrain thermodynamic profile information reasonably well, the results described in this study show that DSD and RF variations still provide significant changes for surface LWF outcomes. Since direct DSD observations are quite scarce and riming factor information is nearly unknown, assumptions will likely be necessary. However, if better DSD and RF parameters are input into the SBC, then case studies of the SBC surface liquid-water fraction can be verified against high-resolution model precipitation types.

6. ACKNOWLEDGMENTS

The authors would like to thank Daphne LaDue for her efforts in putting together an outstanding REU program. This work was prepared by the authors with funding provided by National Science Foundation Grant No. AGS-1062932, and NOAA/Office of Oceanic and Atmospheric Research under NOAA-University of Oklahoma Cooperative Agreement #NA11OAR4320072, U.S. Department of Commerce. The statements, findings, conclusions, and recommendations are those of the author(s) and do not necessarily reflect the views of the National Science Foundation, NOAA, or the U.S. Department of Commerce.

7. REFERENCES

Lundquist, J. D., P. J. Neiman, B. E. Martner, A. B. White, D. J. Gottas, and F. M. Ralph, 2008: Rain versus snow in the Sierra Nevada, California: Comparing Doppler profiling radar and surface observations of melting level. *J. Hydrometeor.,* **9**, 194–211.

Martner, B. E., S. E. Yuter, A. B. White, S. Y. Matrosov, D. E. Kingsmill, and F. M. Ralph, 2008: Raindrop size distributions and rain characteristics in California coastal rainfall for periods with and without a radar bright band. *J. Hydrometeor.,* **9**, 408–425.

Minder, J. R., D. R. Durran, and G. H. Roe, 2011: Mesoscale controls on the mountainside snow line, *J. Atmos. Sci.*, **68**, 2107–2127.

——, and D. E. Kingsmill, 2013: Mesoscale variations of the atmospheric snow line over the northern Sierra Nevada: Multiyear statistics, case study, and mechanisms. *J. Atmos. Sci.,* **70**, 916-938.

Reeves, H. D., A. V. Ryzhkov, J. M. Krause, and W. M. Bartolini, 2015: Discrimination between winter precipitation types based on spectral-bin microphysical modeling. In preparation.

White, A. B., D. J. Gottas, E. T. Strem, F. M. Ralph, and P. J. Neiman, 2002: An automated brightband height detection algorithm for use with Doppler radar spectral moments. *J. Atmos. Oceanic Technol.,* **19**, 687–697.